J. Astrophys. Astr. (2022) 43:66
https://doi.org/10.1007/s12036-022-09860-5

TRANSIENTS

Modeling the late-time merger ejecta emission in short gamma ray bursts

ANKUR GHOSH[1,2,*], KUNTAL MISRA[1], S. V. CHERUKURI[3,4], L. RESMI[3], K. G. ARUN[5], AMITESH OMAR[1], DIMPLE[1] and N. K. CHAKRADHARI[2]

[1]Aryabhatta Research Institute of Observational SciencES (ARIES), Nainital 263001, India.
[2]Department of Physics, Pt. Ravi Shankar Shukla University, Raipur 492010, India.
[3]Indian Institute of Space Science and Technology (IIST), Thiruvanthapuram 695547, India.
[4]Physical Research Laboratory (PRL), Ahmedabad 380009, India.
[5]Chennai Mathematical Institute, Siruseri 603103, India.
*Corresponding author. E-mail: ghosh.ankur1994@gmail.com

MS received 5 January 2022; accepted 25 April 2022

Abstract. The short gamma ray bursts (GRBs) are the aftermath of the merger of binary compact objects (neutron star–neutron star or neutron star–black hole systems). With the simultaneous detection of gravitational wave (GW) signal from GW 170817 and GRB 170817A, the much-hypothesized connection between GWs and short GRBs has been proved beyond doubt. The resultant product of the merger could be a millisecond magnetar or a black hole depending on the binary masses and their equation of state. In the case of a magnetar central engine, fraction of the rotational energy deposited to the emerging ejecta produces late-time synchrotron radio emission from the interaction with the ambient medium. In this paper, we present an analysis of a sample of short GRBs located at a redshift of $z \leq 0.16$, which were observed at the late-time to search for the emission from merger ejecta. Our sample consists of seven short GRBs, which have radio upper limits available from very large array and Australian telescope compact array observations. We generate the model light curves using the standard magnetar model incorporating the relativistic correction. Using the model light curves and upper limits we constrain the number density of the ambient medium to be 10^{-5}–10^{-3} cm^{-3} for rotational energy of the magnetar $E_{\rm rot} \sim 5 \times 10^{51}$ erg. Variation in ejecta mass does not play a significant role in constraining the number density.

Keywords. Gravitational waves—surveys—gamma-ray burst: general—stars: magnetars—stars: neutron.

1. Introduction

The most accepted progenitor model for the origin of short GRBs is the merger of binary compact objects (binary neutron stars (BNS) and neutron star–black hole (NS–BH)). These systems are also the prime candidates for producing gravitational waves and kilonovae. The joint detection of the GW 170817, GRB 170817A and AT2017gfo confirmed the connection among the three events (Abbott *et al.* 2017; Valenti *et al.* 2017; Savchenko *et al.* 2017; Andreoni *et al.* 2017; Drout *et al.* 2017; Tanvir *et al.* 2017). The most debated open question regarding the central engine of GRB is whether black hole, production is necessary for the emergence of short GRB jet or the central engine could be a highly magnetized and rapidly spinning magnetar (Zhang & Mészáros 2001; Metzger *et al.* 2008). In case of a BNS merger, the nature of the remnant depends on the initial masses of the BNS and the equation of state of the NSs. The massive binaries ($\geq 3\,M_{\odot}$) will directly collapse to a black hole whereas the less massive BNS merger creates a transient state in between the merger and the production of black hole which is a millisecond magnetar. In the Swift era, the X-ray light curves from X-ray telescope (XRT, Gehrels *et al.* 2004) show a complex light curve morphology with an early-time X-ray excess (≤ 10 s), mid time flattening or plateau (10–1000 s) and late time X-ray excess followed by a sharp decay (≥ 1000 s). The plateau phase in the X-ray light curves is thought to be powered by the magnetar (Rowlinson *et al.* 2013).

This article is part of the Special Issue on "Astrophysical Jets and Observational Facilities: A National Perspective".

Published online: 13 September 2022

The energy extraction from the central engine occurs via two channels. The first is through the emerging jets from the central engine which carries an enormous amount of energy and gets decelerated by the interaction with the nearby ambient medium. This emission is responsible for the prompt emission and afterglow of the GRBs. Another mode of energy injection is governed by the isotropic ejecta emerging after the merger. As the ejecta is neutron-rich, the matter released during the merger undergoes rapid neutron capture (*r*-process nucleosynthesis) producing heavy elements. The radioactive decay of these heavy and unstable elements power the isotropic and thermal emission known as kilonova (Yu *et al.* 2013; Metzger & Fernández 2014; Metzger 2017). The kilonova ejecta is comparatively much slower than the jet and this mildly relativistic ejecta interacts with the ambient medium on the timescale of nearly a few years since the explosion depending on the energy injection from the central engine as well as the density of the medium (Nakar & Piran 2011). If the resultant product of the merger is a millisecond magnetar, the ejecta would be energized because of the continuous energy injection from the magnetar through the spin-down process. This energized ejecta inevitably crashes into the ambient medium resulting in a long-lived synchrotron emission which peaks in the radio (cm) bands. Late-time observations are therefore, important to detect this emission which will not only help to get a complete picture of the central engine, but will also allow to put constraints on the nature of the ambient medium (Nakar & Piran 2011; Metzger & Bower 2014).

In the past, a few studies have been carried out by Metzger & Bower (2014), Horesh *et al.* (2016), Fong *et al.* (2016), Schroeder *et al.* (2020) and Ricci *et al.* (2021) using the late time observations acquired with the very large array (VLA) and Australian telescope compact array. All these observations were performed at a frequency of 1.4 GHz or more. The upper limits of flux density quoted in the study by Metzger & Bower (2014) were quite high and they concluded that the number density value of $n_0 \leq 10^{-1}$ cm^{-3} can be constrained for a stable magnetar remnant with the rotational energy of $E_{\rm rot} \sim 10^{53}$ erg. The study by Horesh *et al.* (2016) and Fong *et al.* (2016) constrained the number density to be $n_0 \leq 10^{-3}$ cm^{-3} for a large magnetar rotational energy of $E_{\rm rot} \sim 10^{53}$ erg and ejecta mass of $M_{ej} \sim 10^{-2}\ M$. In Schroeder *et al.* (2020) and Ricci *et al.* (2021), the ambient medium density was constrained between 2×10^{-3} and 2×10^{-1} cm^{-3} for the maximum rotational energy of magnetar $\leq 10^{52}$ erg and ejecta mass of $\leq 0.12\ M_{\odot}$.

We have carried out a comprehensive study with a sample of short GRBs up to the year 2017 which lie at a redshift of $z \leq 0.16$. Owing to the small distance where these bursts lie, they are ideal candidates for detecting any late-time emission from the merger ejecta. We assume that these events are the results of BNS merger and with the availability of detection upper limits, our model will allow to put stringent constraints on the remnant and ambient medium properties. In our model, we use the basic magnetar model taking into account the energy injection from the central engine, evolution of the synchrotron frequencies and generic hydrodynamics as well as propose modifications by incorporating the relativistic correction due to the evolution of the bulk Lorentz factor. A detailed discussion of our model is presented in Section 3.

The paper is organized as follows. In Section 2, we discuss the sample selection of short GRBs. Section 3 describes our model and the modifications we have incorporated as compared to the other previous studies. In Section 4, we provide model parameters for the selected bursts and conclude our findings in Section 5. Throughout the paper, we assume a ΛCDM cosmology with $H_0 = 70$ km s^{-1} Mpc^{-1}, $\Omega_m = 0.27$ and $\Omega_\Lambda = 0.73$ (Komatsu *et al.* 2011).

2. Sample selection

We choose short GRBs in the local universe with spectroscopic redshift up to 0.16 and those showing a plateau phase in their X-ray light curves. The previous studies by Fong *et al.* (2016), Schroeder *et al.* (2020) and Ricci *et al.* (2021) present late-time data of short GRBs which exibhit a plateau phase in their X-ray light curves. We select GRBs from these studies, which have observations at 2.1 and 6.0 GHz. Seventeen GRBs in the literature show a plateau in their X-ray light curves. Among these, only seven GRBs lie within the redshift up to 0.16. GRB 170817A located at a very low redshift of 0.0097 is also included in our sample. The observational details of seven GRBs in our sample are given in Table 1.

3. Magnetar modeling

The late-time radio emission in short GRBs powered by magnetars is a result of the interaction between the tidally disrupted ejecta and the

Table 1. Observational details of seven GRBs in our sample.

GRB	Redshift (z)	Frequency band (GHz)	$T^{1}_{\rm obs}$ (yrs)	3σ upper limit (μJy)	X-ray behavior	References
060614	0.125	2.1	9.41	252	Extended emission	Yang *et al.* (2015)
		2.1	0.92	150		Horesh *et al.* (2016)
061201	0.111	2.1	8.91	351		Stratta *et al.* (2007)
080905	0.122	2.1	7.37	537	Early steep decline	Rowlinson *et al.* (2010)
		6.0	5.77	61.8	Early steep decline	Fong *et al.* (2016)
		6.0	6.47	57		Rowlinson *et al.* (2010)
130822A	0.154	2.1	2.18	270	Early steep decline	Ricci *et al.* (2021)
		6.0	5.38	27	Early steep decline	Ricci *et al.* (2021)
150101B	0.1341	2.1	0.82	234	Off-axis	Troja *et al.* (2018)
		6.0	3.03	99	Off-axis	Troja *et al.* (2018)
160821B	0.1613	6.0	2.38	18	Early steep decline	Troja *et al.* (2019)
170817A	0.0097	6.0	1.98	24.2	Extended emission	Hajela *et al.* (2016)

$T^{1}_{\rm obs}$ is calculated since burst trigger time.

ambient medium (Nakar & Piran 2011). The first consideration is that the ejecta is emerging spherically from the central engine with an initial velocity β_0. The emission from the ejecta is characterized by several parameters like ejecta mass M_{ej}, rotational energy of the magnetar $E_{\rm rot}$, ambient medium density n_0, the fraction of post-shock energy into the accelerating electrons and magnetic field ϵ_e and ϵ_B, respectively, and the power-law distribution index of electrons p with $N(\gamma) \propto \gamma^{-p}$. The simplistic magnetar modeling has earlier been used in Nakar & Piran (2011), Metzger & Bower (2014), Horesh *et al.* (2016), Fong *et al.* (2016), where they included the energy injection from the central engine and the synchrotron self-absorption effect. Some modifications like generic hydrodynamics and deep Newtonian phase were proposed in Liu *et al.* (2020), Schroeder *et al.* (2020) and Ricci *et al.* (2021). However, none of these models consider the evolution of the bulk Lorentz factor. We discuss the magnetar model in detail below, incorporating the relativistic correction.

3.1 *Ejecta dynamics*

The rotational energy of the stable NS remnant formed in a BNS merger can be calculated using

$$E_{\rm rot} = \frac{1}{2} I \Omega^2 \simeq 3 \times 10^{52}\ {\rm erg} \left(\frac{P}{1\ {\rm ms}}\right)^{-2}, \qquad (1)$$

where $I \simeq 1.5 \times 10^{15}$ g cm^{-3} is the moment of inertia of a NS. In the presence of a magnetar central engine, a significant fraction of its rotational energy is transferred to the ejecta, which acts as a driving force behind the acceleration of the ejecta (Nakar 2007).

To calculate the deceleration radius and timescale, it is mandatory to consider the evolution of the bulk Lorentz factor (Γ) of the ejecta with the swept up mass (M_s) as described in Pe'er (2012) and is shown below:

$$\frac{{\rm d}\Gamma}{{\rm d}M_s} = -\frac{\hat{\gamma}(\Gamma^2 - 1) - (\hat{\gamma} - 1)\Gamma\beta^2}{M_{ej} + M_s[2\hat{\gamma}\Gamma - (\hat{\gamma} - 1)(1 + \Gamma^{-2})]}, \qquad (2)$$

where $\hat{\gamma}$ is the adiabatic index, M_{ej} is the ejecta mass and β is the velocity of the ejecta.

The evolution of swept-up mass from ambient medium (M_s) and ejecta radius (r) are given in Pe'er (2012) as follows:

$$\frac{{\rm d}M_s}{{\rm d}r} = 4\pi r^2 n_0 m_p \qquad (3)$$

and

$$\frac{{\rm d}r}{{\rm d}t} = \Gamma^2 \beta(\Gamma) c(1 + \beta(\Gamma)), \qquad (4)$$

where m_p is the mass of proton and n_0 is the density of the ambient medium.

On solving Equations (2)–(4), we obtain expressions for Γ, swept-up mass M_s and radius.

Initially, there is an enhancement in the kinetic energy of the ejecta because of continuous energy injection from the magnetar. When the ejecta collects a mass comparable to its own from the ambient medium, the ejecta starts decelerating at the characteristic timescale ($t_{\rm dec}$) and radius ($R_{\rm dec}$). To calculate

$t_{\rm dec}$ and $R_{\rm dec}$, we have considered a spherical outflow from the central engine with the rotational energy ($E_{\rm rot}$) of the magnetar and initial Lorentz factor (γ_0) with the associated velocity $c\beta_0$, which propagates through the CSM of density n_0:

$$R_{\rm dec} \simeq \left(\frac{3E_{\rm rot}}{4\pi n_0 m_p c^2 \gamma_0(\gamma_0-1)}\right)^{1/3} \tag{5}$$

and

$$t_{\rm dec} \sim \frac{R_{\rm dec}(1-\beta_0)}{c\beta_0}. \tag{6}$$

The minimum Lorentz factor (γ_m) and the magnetic field strength (B) in the shock can be calculated using the fraction of energy transferred to the electron energy and magnetic field (ϵ_e and ϵ_B), respectively.

$$\gamma_m = 1 + \left(\frac{p-2}{p-1}\right)\frac{m_p}{m_e}\epsilon_e(\Gamma-1) \tag{7}$$

and

$$B = c(32\pi n_0 m_p \epsilon_B \Gamma(\Gamma-1))^{1/2}. \tag{8}$$

3.2 *Calculation of synchrotron frequencies*

The late-time radio spectrum is completely dominated by two frequencies. One of them is the typical synchrotron frequency ν_m of the electrons having the minimum Lorentz factor γ_m:

$$\nu_m = \left(\frac{3q}{4\pi m_e c}\right) B\gamma_m^2 \Gamma(1+z)^{0.5}, \tag{9}$$

where q and m_e are charge and mass, respectively, of the electron, c is the velocity of light, B is the magnetic field and z is the redshift of the GRB.

The other is the synchrotron self-absorption frequency ν_a. Radio emission becomes observable when the observed frequency is above ν_a. ν_a plays a very significant role in low frequency radio regime. The expression for ν_a from Nakar & Piran (2011) is shown below:

$$\nu_a \approx 1\ {\rm GHz}\left(\frac{R}{10^{17}}\right)^{\frac{2}{(p+4)}}\left(\frac{\epsilon_B}{0.1}\right)^{\frac{2+p}{2(p+4)}} \times \left(\frac{\epsilon_e}{0.1}\right)^{\frac{2(p-1)}{p+4}} n^{\frac{6+p}{2(p+4)}}\beta_0^{\frac{5p-2}{p+4}}. \tag{10}$$

Another important frequency in the synchrotron spectrum is the cooling frequency ν_c. For the late-time emission scenario, ν_c lies much above the observable frequency, and ν_m and ν_a. The contribution of ν_c in the late-time radio light curves is therefore not significant.

3.3 *Synchrotron flux calculation*

If the observing frequency is greater than ν_m and ν_a, then, the corresponding observed peak flux density can be calculated from Wijers & Galama (1999). The specific flux f_ν of a single electron can be written as

$$F_{\nu,e} = \frac{P_{\nu,e}}{4\pi d_L^2}, \tag{11}$$

where $P_{\nu,e}$ is the power emitted by a single electron per unit frequency in rest frame and d_L is the distance to the source. $P_{\nu_m,e}$ can be written as (Wijers & Galama 1999):

$$P_{\nu_m,e} = \phi_p \frac{\sqrt{3}e^3 B}{m_e c^2}, \tag{12}$$

where ϕ_p is the flux of the dimensionless maximum point of the spectrum ($f(x_p) = \phi_p$). e and m_e are representing the electron charge and mass, respectively.

After accounting for the redshift and relativistic transformation, the total specific flux, $F_{\nu_m,{\rm obs}}$, can be written as:

$$F_{\nu_m,{\rm obs}} = \frac{N_e P_{\nu_m,e}\Gamma(1+z)}{4\pi d_L^2}. \tag{13}$$

Here, we consider that the ejecta is ploughing through the constant density inter-stellar medium (ISM), then, we can write $N_e = 4/3\pi R^3 n$. Substituting N_e and Equation (12) in Equation (13), we evaluate the total specific flux as

$$F_{\nu_m,{\rm obs}} = \frac{\sqrt{3}Be^3}{m_e c^2}\frac{R^3 n_0 \Gamma(1+z)}{3d_L^2}. \tag{14}$$

Substituting Equation (8) in Equation (14), we obtain the final flux equation in terms of n and ϵ_B.

$$F_{\nu_m,{\rm obs}} = \frac{\sqrt{96\pi n_0^3 m_p \epsilon_B \Gamma^3(\Gamma-1)}}{m_e c}\frac{R^3 e^3(1+z)}{3d_L^2}. \tag{15}$$

4. Light curve analysis

Using the above formulation, we generate the model light curves and compare them with the 3σ upper limits. While constructing the model light curves, we

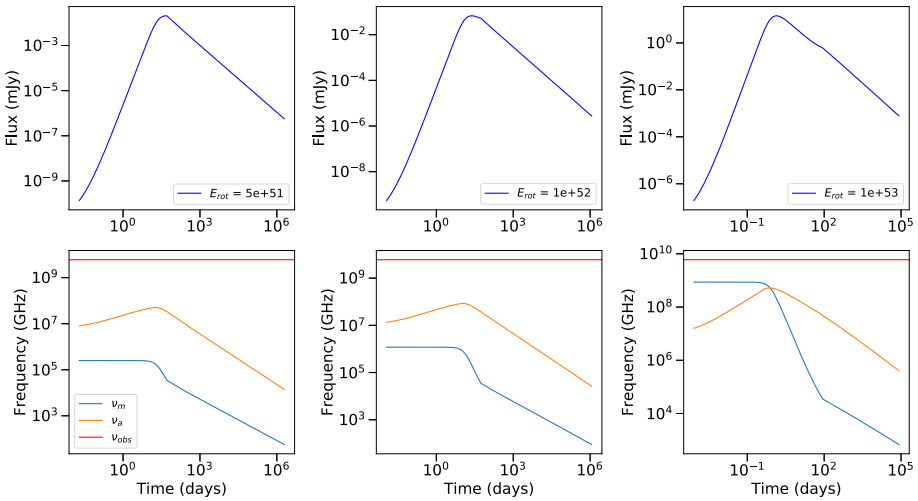

Figure 1. Model light curves and the evolution of ν_a and ν_m. The ejecta mass is fixed at 0.04 $M_\odot$ and number density of the ambient medium is fixed at 10^{-2} cm^{-3}. The solid horizontal lines in the bottom panels indicate the observed frequency.

take into account the assumptions and fiducial values of certain parameters described below:

- Numerical simulations showed that long-lived merger remnants eject a large fraction of the remnant accretion disk mass (Metzger & Fernández 2014). We consider ejecta mass values of 0.04 $M_\odot$ and 0.1 $M_\odot$, which corresponds to velocities $\beta \sim 0.5$ and 0.3, respectively. Velocities below $\beta < 0.3$ are discarded because they will produce very weak and delayed radio emission.
- We varied the magnetar rotational energy from 10^{51} to 10^{53} erg. The upper limit of rotational energy corresponds to a stable neutron star of mass 2.2 $M_\odot$ (Metzger *et al.* 2015).
- The fraction of post-shock energy into the accelerating electron ϵ_e is fixed at 0.1.
- The fraction of post-shock energy into the magnetic field ϵ_B is at 0.1 and 0.01.
- The powerlaw index p is fixed at 2.4.
- The density of the ambient medium is not fixed. It generally varies in a vast range for different GRBs. We take the number density range between 10^{-5} and 1 cm^{-3} in six equal intervals.

The top panel of Figure 1 show the model light curves for different values of rotational energy (5×10^{51}–10^{53} erg) for a fixed ejecta mass (0.04 $M_\odot$) and number density (10^{-2} cm^{-3}) at a frequency of 6 GHz. The evolution of ν_a and ν_m is shown in the bottom panel. ν_m, which represents the average kinetic energy of the radiating electrons remains below ν_a for lower values of rotational energy. But for higher rotational energy, the electron population achieves higher γ_m, leading to ν_m to exceed ν_a. The peak of the model light curves is consistent with the peak of ν_m. At late times, the role of ν_c is insignificant as it lies much beyond the observable frequencies.

Figures 2–4 show the model light curves along with the 3σ upper limits from VLA and ATCA of the GRBs in our sample (Table 1). The models are generated for different values of ejecta mass, ϵ_B, magnetar rotational energy and number density as indicated in the Figures. The model light curves in these Figures depict that the peak time of the light curves are decreasing with increasing values of rotational energy of the magnetar and the ambient medium density. In addition to that, the model flux decreases for increasing values of ejecta mass and decreasing values of magnetar rotational energy.

From Figures 2 and 3 it is evident that the most energetic scenario ($E_{\rm rot} \sim 10^{53}$ erg) is disfavoured as the upper limits lie beyond the model light curves and would require much smaller ambient medium density ($< 10^{-5}$ cm^{-3}) and ϵ_B (< 0.01) to satisfy the observational constraints. In a study by Ricci *et al.* (2021), it was found that the number densities are better constrained for GRBs at lower redshifts as compared to those lying at higher redshifts. In our sample of low redshift short GRBs, the models with ambient medium densities of $n_0 \geq 10^{-4}$ cm^{-3} are ruled out for magnetar rotational energy of 10^{52} erg. Models with rotational energy $\sim 5 \times 10^{51}$ erg constrains the number density values within 10^{-5}–10^{-3} cm^{-3}. The number density obtained in this work is consistent with the previous studies by Ricci *et al.* (2021).

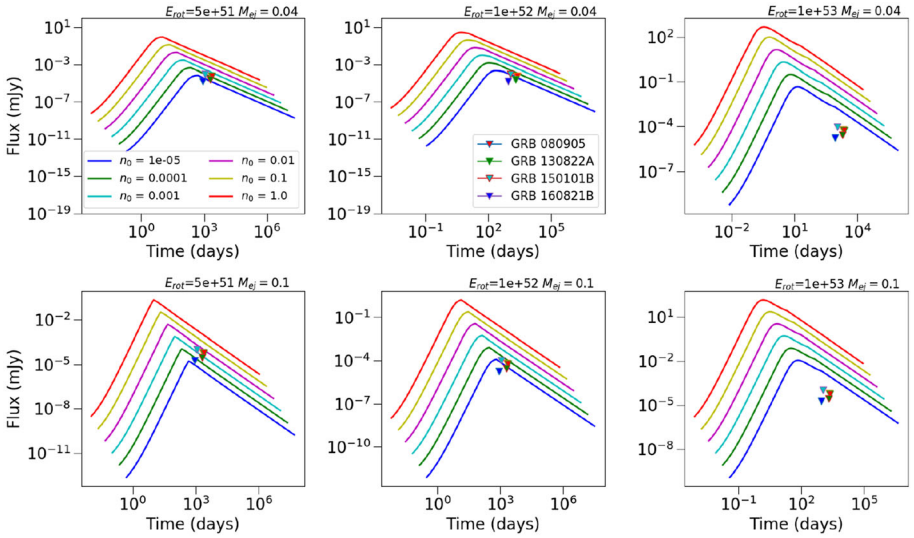

Figure 2. Model light curves along with the VLA 6 GHz 3σ upper limits. The upper limits are shown as inverted triangles in the figure. The value of ϵ_B is fixed to 0.1. For two different values of ejecta mass 0.04 and 0.1 $M_\odot$, we generate the model light curves with different magenetar rotational energy and number density as indicated in the plot.

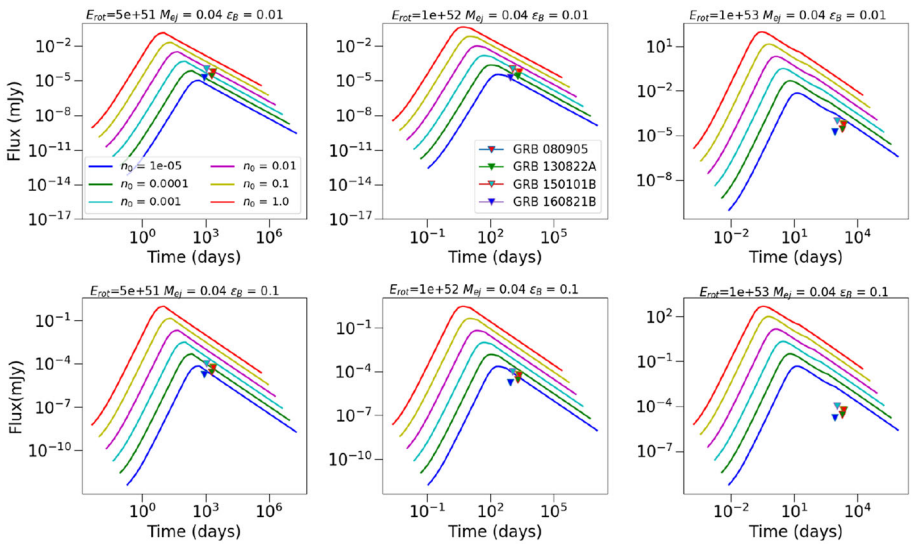

Figure 3. Same as Figure 2, but for a fixed value of ejecta mass and two different values of ϵ_B (0.01 and 0.1).

The model light curves with high rotational energy (10^{53} erg) and lower value of $\epsilon_B = 0.01$ are satisfied only for very low number density values ($n_0 \leq 10^{-5}$ cm^{-3}). However, for lower magnetar rotational energy (10^{51} and 10^{52} erg), stringent constraints for number density values (between 10^{-4} and 10^{-2} cm^{-3}) have been found.

In Figure 5, we show the model light curves, generated for fixed values of ejecta mass and ϵ_B considering different values of rotational energy and number density along with the 3σ upper limit of GRB 170817A. The upper limit available is at $\sim$714 days since the burst. The available upper limit does not satisfy any of the models indicating that different values of the parameters may be required to generate the models. Further late-time monitoring of GRB 170817A would be useful to search for the emission at late-time due to merger ejecta.

5. Conclusions

A faint radio emission is expected when the merger ejecta collides with the ambient medium in the presence of a magnetar central engine (Nakar & Piran 2011). Several studies in the past have reported upper limits in a quest to search for merger ejecta emission

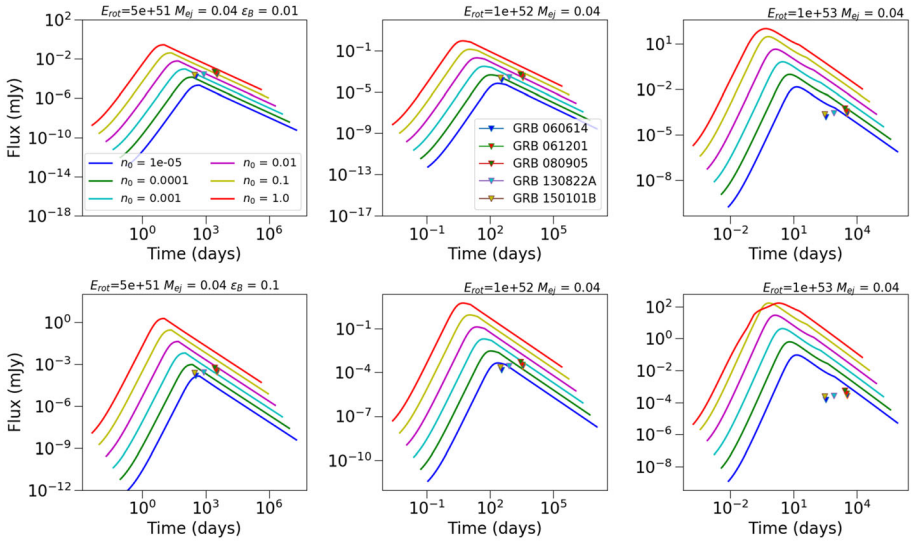

Figure 4. Model light curves along with the ATCA 2.1 GHz 3σ upper limits. The model light curves are generated for a fixed ejecta mass and two different values of ϵ_B (0.01 and 0.1).

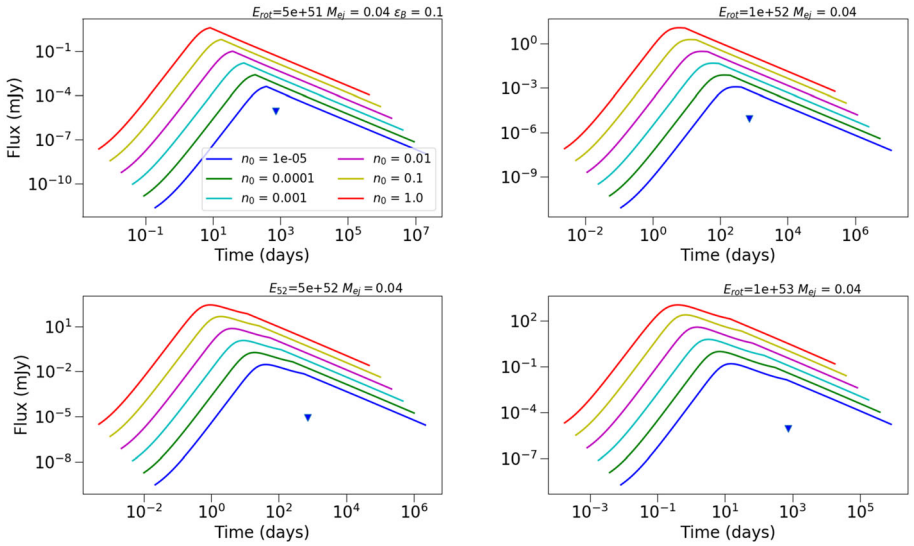

Figure 5. Model light curves along with the VLA 6 GHz 3σ upper limit of GRB 170817A. The ejecta mass and ϵ_B values are fixed at 0.04 $M_\odot$ and 0.1, respectively.

in radio bands from short GRBs (Metzger & Bower 2014; Fong *et al.* 2016; Horesh *et al.* 2016; Schroeder *et al.* 2020; Ricci *et al.* 2021). The upper limits are very useful to constrain the ambient medium density and the rotational energy of the magnetar. We select a sample of seven short GRBs located at a redshift of $z \leq 0.16$ for which upper limits were reported in the literature. We used the standard magnetar model and modified it to incorporate the relativistic corrections. The model light curves thus generated are used to constrain the basic parameters of the central engine and ambient medium.

We find that models with high rotational energy are disfavoured, whereas models with lower values of rotational energy provide tight constraints on the ambient medium density ($n_0 \sim 10^{-5}$–10^{-3} cm^{-3}) except the ATCA 2.1 GHz light curves for $\epsilon_B = 0.01$. The number density values obtained are very low. It is also seen that changing the ejecta mass does not have much effect on the late-time light curves. The radio emission from merger ejecta is expected to peak at the deceleration time (typically after a few years since the burst). Therefore, observations not very far out in time, will not be able to detect any radio emission, if

any. It is important to acquire observations at late-time. In the case of GRB 170817A, the model light curves are unable to explain the radio upper limits. Late-time observations of GRB 170817A could substantially refine these constraints.

In the near future, it may be possible to detect merger ejecta emission from near by local short GRBs with the next generation radio telescopes and prove the existence of magnetar central engine. The upcoming radio telescopes like the square kilometer array (SKA) and new generation VLA (ng-VLA) with increased sensitivity of μJy level will push the detection limits of merger ejecta emission at late time.

Acknowledgements

KM acknowledges BRICS grant DST/IMRCD/BRICS/PilotCall1/ProFCheap/2017(G) for the financial support. KGA is partially supported by the Swarnajayanti Fellowship Grant No. DST/SJF/PSA-01/2017-18, MATRICS Grant MTR/2020/000177 of SERB and a grant from the Infosys Foundation.

References

Abbott B. P., Abbott R., Abbott T. D., *et al.* 2017, The Astrophysical Journal Letters, 848, L13

Andreoni I., Ackley K., Cooke J., *et al.* 2017, Publications of the Astronomical Society of Australia, 34, e069

Drout M. R., Piro A. L., Shappee B. J., *et al.* 2017, Science, 358, 1570

Fong W., Metzger B. D., Berger E., Özel F. 2016, The Astrophysical Journal, 831, 141

Gehrels N., Chincarini G., Giommi P., *et al.* 2004, The Astrophysical Journal, 611, 1005

Hajela A., Margutti R., Alexander K. B., *et al.* 2016, The Astrophysical Journal Letters, 831, 141

Horesh A., Hotokezaka K., Piran T., Nakar E., Hancock P. 2016, The Astrophysical Journal Letters, 819, L22

Komatsu E., Smith K. M., Dunkley J., *et al.* 2011, The Astrophysical Journal Supplement Series, 192, 18

Liu L.-D., Gao H., Zhang B. 2020, The Astrophysical Journal, 890, 102

Metzger B. D. 2017, Living Reviews in Relativity, 20, 3

Metzger B. D., Bower G. C. 2014, Monthly Notices of the Royal Astronomical Society, 437, 1821

Metzger B. D., Fernández R. 2014, Monthly Notices of the Royal Astronomical Society, 441, 3444

Metzger B. D., Margalit B., Kasen D., Quataert, E. 2015, Monthly Notices of the Royal Astronomical Society, 454, 3311

Metzger B. D., Quataert E., Thompson T. A. 2008, Monthly Notices of the Royal Astronomical Society, 385, 1455

Nakar E. 2007, Physics Reports, 442, 166

Nakar E., Piran T. 2011, Nature, 478, 82

Pe'er A. 2012, The Astrophysical Journal Letters, 752, L8

Ricci R., Troja E., Bruni G., *et al.* 2021, Monthly Notices of the Royal Astronomical Society, 500, 1708

Rowlinson A., O'Brien P. T., Metzger B. D., Tanvir N. R., Levan A. J. 2013, Monthly Notices of the Royal Astronomical Society, 430, 1061

Rowlinson A., Wiersema K., Levan A. J., *et al.* 2010, Monthly Notices of the Royal Astronomical Society, 408, 383

Savchenko V., Ferrigno C., Kuulkers E., *et al.* 2017, The Astrophysical Journal Letters, 848, L15

Schroeder G., Margalit B., Fong W.-F., *et al.* 2020, The Astrophysical Journal, 902, 82

Stratta G., D'Avanzo P., Piranomonte S., *et al.* 2007, Astronomy and Astrophysics, 474, 827

Tanvir N. R., Levan A. J., González-Fernández C., *et al.* 2017, The Astrophysical Journal Letters, 848, L27

Troja E., Ryan G., Piro L., *et al.* 2018, Nature Communications, 9, 4089

Troja E., Castro-Tirado A. J., Becerra González J., *et al.* 2019, Monthly Notices of the Royal Astronomical Society, 489, 2104

Valenti S., Sand D. J., Yang S., *et al.* 2017, The Astrophysical Journal Letters, 848, L24

Wijers R. A. M. J., Galama T. J. 1999, The Astrophysical Journal, 523, 177

Yang B., Jin Z.-P., Li X., *et al.* 2015, Nature Communications, 6, 7323

Yu Y.-W., Zhang B., Gao H. 2013, The Astrophysical Journal Letters, 776, L40

Zhang B., Mészáros P. 2001, The Astrophysical Journal Letters, 552, L35